EXPERIMENTAL AND MODELLING STUDY ON OPTIMIZATION OF GLASS FIBER FILTER DIVERSION STRUCTURE

Lele Zhang, Liang HU, Jing HU, Jianmin Zhao*, Yangui Chen, Jieqing Zheng

Key Laboratory of Energy Cleaning Utilization and Development of Fujian Province, Jimei University, Xiamen, 361021, Fujian, China;

* Jianmin Zhao; E-mail: zjm@jmu.edu.cn

This study conducts an experimental and modeling investigation on the optimization of the glass fiber filter diversion structure. Addressing the critical issue in air filtration systems of enhancing the service life and performance of filter devices, this research rationally designs and optimizes the structural parameters of the diversion structure. Numerical simulation of the filter device was established through airflow organization experiments of glass fiber filters to explore the impact of various guide vane structure parameters on the system's air distribution uniformity and service life. Furthermore, machine learning was employed to optimize the guide structure of the filtration device based on the results of numerical simulations. The study demonstrates a good agreement between numerical simulation results and experimental outcomes, with an error of less than 10%. The optimal length and angle of the guide plate predicted by machine learning are 163.2 mm and 38.5°, respectively. This research not only injects new momentum into the continuous advancement of air filtration technology but also shows significant potential in energy efficiency and cost control.

Key words*: Air Filtration Systems, Diversion Structure, Numerical Simulation, Machine Learning.*

1. Introduction

In light of the escalating environmental contamination and industrialization, coupled with the recurrent influenza epidemics, air pollution has emerged as a critical issue of the 21st century [1, 2]. With the majority of human activity, an estimated 80-90%, confined to indoor settings, indoor air quality (IAQ) has risen to become one of the top three public health hazards [3]. Therefore, the deployment of effective air filtration systems is paramount in the strategy to ensure public health by achieving in-depth air purification and maintaining optimal IAQ.

At present, effective air filtration devices are used in medical [4, 5], transportation [6, 7] as well as residential [8, 9] or industrial applications. However, the continuous operation of air filters is prone to accumulate dust cakes, resulting in increased resistance and energy waste [10]. To promote the concept of green sustainable development and effectively balance filtration performance and energy consumption, scholars in related fields have explored scientific pathways to improve indoor air quality from perspectives such as air purification technology, pollution source simulation experiments and optimized design of air supply systems.

The reduction of pollutant concentration can be effectively managed with the help of diversified purification technologies [11], such as traditional dry filtration [12], ultraviolet irradiation [13], photocatalytic degradation [14], dynamic plant filtration systems [15], and air purification systems such as plasma [16]. Among them, traditional dry filtration, such as fibre filtration [17], is widely used due to its low cost and ease of production.

To enhance the efficiency and service life of dry filtration systems, the current research mainly focuses on the optimization of filter elements and the design of diversion structures. Initially, First of all, the optimal design of the filter element is closely related to its material, pleat number, geometric characteristics and other factors [18]. Antuo Wang et al. [19] improved filtration performance by controlling the porous structure on the surface of fibers through the fabrication of PTFE porous fibrous membranes. Li et al. [20] analyzed the impact of pleat geometry on the filtration and cleaning characteristics of filter media, highlighting that the effective filtration area is predominantly influenced by the pleat ratio. Alilou et al. [21] explored the influence of pleats on the air velocity field within HEPA filters by using CFX and GeoDict. Guangping Teng et al. [22] further explained the advantages of U-shaped filters in filtration performance by establishing a pressure drop model during the dust loading process. However, compared to the substantial achievements in filter element optimization, research on the optimization of flow-guiding structures remains limited, with only a few scholars making preliminary progress in this area. Zhang et al. [23] pointed out that adding flow-guiding devices can improve the uniformity index of the airflow field by over 5%. Zhuang et al. [24] used a comprehensive evaluation metric of thermal efficiency and effective efficiency to analyze the impact of V-shaped perforated baffle structures, which incorporate solar air heaters, on performance, identifying the optimal structural parameters for the guiding plates. Menni et al. [25] studied the effects of different flow guide plate shapes on the steady-state turbulent forced convection behavior within air heater channels, concluding that the V-shaped guiding plate represents the best design, with a thermal enhancement factor increased by 13.542% compared to a simple baffle. Therefore, the addition of guiding plates and the optimization of their structures can significantly enhance the uniformity of the airflow field and effectively improve the performance of related equipment.

The structural parameters of diversion devices are diverse, and their effects on filters are complex, leading to high economic and technical costs for experiments [26]. Therefore, researchers have turned to developing precise numerical models to explore the uniformity of airflow fields. For instance, Li et al. [27] utilized numerical simulations to investigate the flow and heat transfer characteristics of turbulent fluid in channels with multiple V-shaped baffles. Luo et al. [28] derived optimal folding distance and height parameters for HEPA filters under different wind speed conditions based on Computational Fluid Dynamics (CFD). Cheng et al. [29] constructed a model of V-shaped pleated air filter media and employed a CFD-Discrete Element Method (DEM) coupling approach to simulate the deposition process on particle model surfaces. Xu et al. [30] conducted a comprehensive evaluation of flow performance and filter utilization in air purifiers by selecting various filter structures and adding inlet diversion features, using Fluent software. Although these studies have achieved certain results in numerical simulation, they generally lack sufficient experimental validation. The limitations in the selection of operating conditions often mean that the proposed optimal design solutions are applicable only under specific circumstances, making broader implementation challenging.

Machine learning, as a significant branch of artificial intelligence, demonstrates immense potential in handling complex data, optimizing decision-making processes and achieving automation [31]. The models it establishes rely on vast amounts of data for training and learning, continuously optimizing themselves through feedback mechanisms [32]. Bayesian-based machine learning methods effectively utilize historical data during the search process, gradually narrowing the search space for optimal solutions, thereby enhancing search efficiency. Although numerical simulation and machine learning each have their advantages, there is limited research on the application of coupling these two methods for optimizing model parameters. Additionally, there is currently a lack of relevant experimental and theoretical validation regarding the efficiency and lifespan of dry filtration in the context of flow structures.

The purpose of this study is to enhance the efficiency and longevity of air filtration systems by optimizing the glass fiber filter diversion structure, with the main work involving experimental analysis of the effects of diffuser dimensions on airflow distribution, simulation modeling using COMSOL software to assess air uniformity and filter utilization, application of machine learning to predict optimal structural parameters, and the development of broadly applicable models that could significantly improve energy efficiency and cost-effectiveness in various sectors.

2. Experimental work

2.1. Materials

The experiment utilized an H14-grade high-efficiency air filter produced by Xingyue Purification Equipment Co., Ltd., with dimensions of 200 × 400 × 45 mm and an initial resistance maintained below 150 Pa. The filter media consists of fiberglass filter paper, designed with a wedge-shaped pleat that is folded on both sides. The frame is made of aluminum alloy and equipped with dual protective grids, resulting in a compact and lightweight structure, as illustrated in the Fig.1. The airflow velocity of the high-efficiency filter, which is the air velocity passing through the filter surface per unit time, is one of the key indicators for assessing its performance and has a direct impact on both filtration effectiveness and resistance. In this experiment, the airflow velocity of the filter was set at 0.45 m/s. To effectively extend its service life, the filter employs a special hot-melt adhesive to separate the filter papers, ensuring uniform and reasonable spacing between them, thereby achieving consistent airflow and low resistance. All components are made from materials with extremely low chemical volatility, meeting the requirements for conventional clean rooms and air filtration equipment.

Fig.1 H14-grade high-efficiency air filter.

The micro-flow within the pore space is uniformly distributed on a macroscopic scale. Porosity, as a crucial parameter in materials science, is defined as the ratio of the volume of pore space within a material to its total volume, which ultimately determines the apparent average flow rate [33]. This parameter is vital for understanding the macroscopic behavior of materials, such as fluid flow and mass transport. To accurately quantify the porosity of the filter core, high-resolution scanning images were obtained using the Phenom XL G2 desktop scanning electron microscope (SEM) from four randomly selected regions of the filter core. Using ImageJ image processing software, threshold algorithms were applied to binarize the images, clearly distinguishing between porous and non-porous areas. The scanning electron microscopy images and their corresponding binarized images are shown in Fig.2.

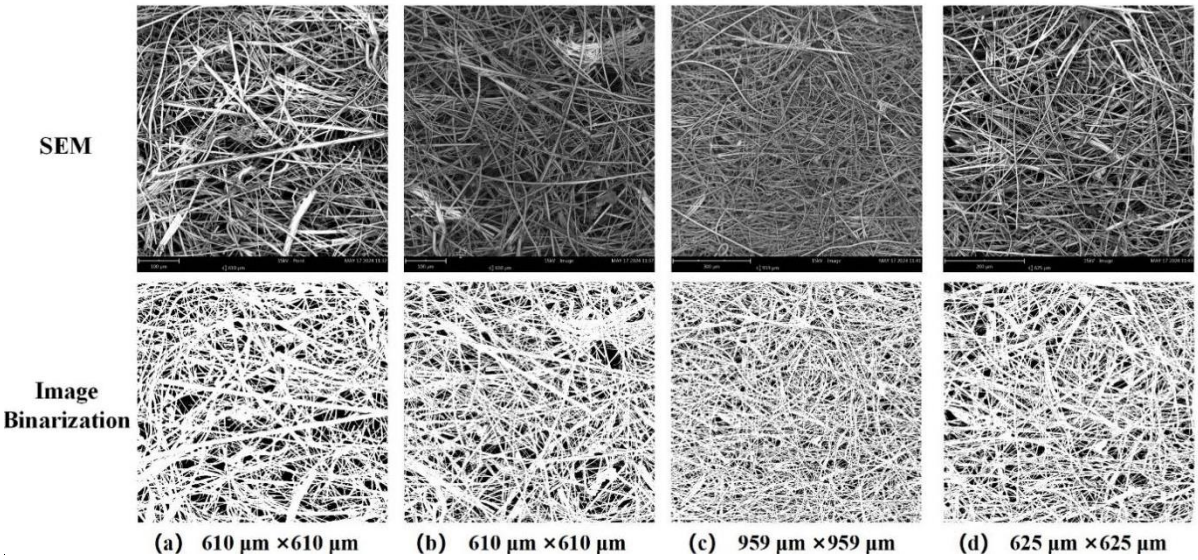

Fig.2 The SEM imaging of the filter element and its binarized images.

After processing, the ratio of the pore area to the total area for each image is presented in Tab. 1. Statistical results indicate that the average porosity of the studied filter core is approximately 0.27.

Tab 1. Image Pore Data.

	Image 1	Image 2	Image 3	Image 4	Average
Pore area (px)	260937	261450	268133	265260	-
Total area (px)	1024×960	1024×960	1024×960	1024×960	-
Porosity	26.54%	26.60%	27.28%	26.98%	26.85%

2.2. Experiment

To investigate the impact of deflector structure parameters on the airflow distribution uniformity within the purifier chamber, this study constructs a physical model containing an air purification module, as shown in Fig.3. The model is made of acrylic material with dimensions of 400 mm in length, 600 mm in width, and 200 mm in height. An H14 high-efficiency air filter is selected to ensure consistent and reasonable spacing between filter media, thereby optimizing the airflow path to achieve uniform velocity distribution and lower flow resistance. The distance from the filter element to the inlet is set at 300 mm. To accurately assess the airflow distribution within the model, five velocity sampling points are established along the model's sidewalls, corresponding to five cross-sections located at 0 mm, 100 mm and 200 mm in front of the filter's windward face, as well as at 0 mm and 150 mm in front of the filter's leeward face, with all sampling points positioned 50 mm above the bottom of the chamber. To reflect the airflow distribution under different deflector structure

parameters, a 120W, 200-2P-220V floor-mounted axial fan is utilized, with airflow rates of 1100-2000 m^3/h. Wind speed measurements are conducted using a Testo hot-wire anemometer at the five cross-sections, taken at lateral distances of 50 mm, 100 mm, 150 mm and 200 mm from the sidewall, yielding a total of 20 precise wind speed data points.

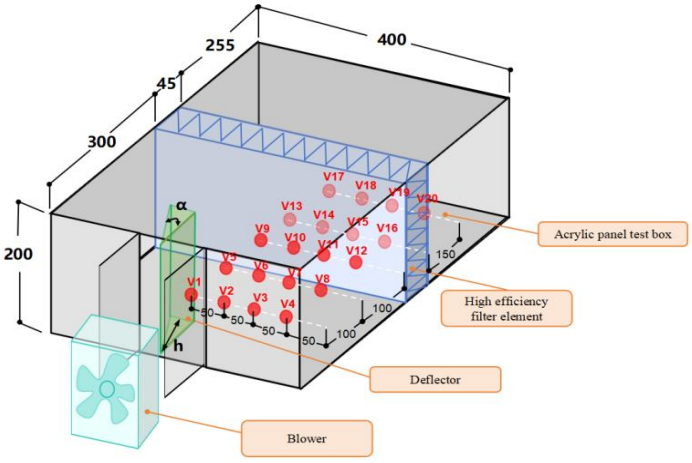

Fig.3 The schematic diagram of the experimental setup.

The study employs an isosceles triangle as the geometric configuration of the deflector, designating the angle α and length h has the key structural parameters. Four distinct angle values (10°, 20°, 30° and 40°) and three different lengths (50 mm, 100 mm and 150 mm) were selected for comparative analysis. To comprehensively evaluate the performance of the deflector, a baseline condition without a deflector was also established. In total, the experiment encompasses 13 different comparative conditions, as shown in Tab.2.

Tab.2 The comparative working conditions.

α / h	0°	10°	20°	30°	40°
0mm	Case 1	-	-	-	-
50mm	Case 2	Case 3	Case 4	Case 5	-
100mm	-	Case 6	Case 7	Case 8	Case 9
150mm	-	Case 10	Case 11	Case 12	Case 13

3. Modeling approach

3.1. Sublimation kinetics model of dry ice

Based on the physical model configuration, this study utilizes COMSOL Multiphysics software for modeling, solving, and analyzing the problem, which has demonstrated significant advantages in exploring the complexities of porous media [34]. To comprehensively and thoroughly investigate the optimal configuration and flow performance of the flow guide plates, a series of combinations of structural parameters for the plates were established. The length of the flow guide plates was set to 10-200 mm (increasing by 10 mm increments), while the angle was set to 10-100° (increasing by 10° increments), resulting in a total of 200 simulation experiments. The results of the numerical simulations form a rich and detailed dataset that will provide a solid foundation for the subsequent learning and optimization of neural networks.

3.1.1 Fundamental Principles of Numerical Simulation

The Reynolds number is a core concept in fluid dynamics, expressed by the following formula:

$$R_e = \frac{\rho v L}{\mu} \tag{1}$$

where, ρ [kgm^{-3}] is the fluid density, v [ms^{-1}] is the fluid velocity, μ [Nsm^{-2}] is the dynamic viscosity of the fluid, L [m] is the characteristic length.

The flow of fluid within the purifier adheres to the continuity equation and the momentum equation [35]. The continuity equation, which is based on the principle of mass conservation, states that the net mass of fluid exiting the control volume per unit time is equal to the mass reduced within the control volume over the time interval due to changes in density. The differential form of the continuity equation can be derived as follows:

$$\frac{\partial \rho}{\partial t} + \frac{\partial (\rho u)}{\partial x} + \frac{\partial (\rho v)}{\partial y} = \frac{\partial \rho}{\partial t} + \nabla \cdot (\rho \boldsymbol{u}) = 0 \tag{2}$$

where, u、v [ms^{-1}] is respectively the velocity components of the fluid in the x and y directions, ρ [kgm^{-3}] is the fluid density, $\mathbf{u}$ is the The velocity vector of the fluid, t [s] is time.

When the fluid flows within the purifier, the flow space remains fixed. In this case, the fluid motion adheres to the conservation of momentum equation, as indicated in Eq. (3), where the rate of change of momentum to time is equal to the sum of various external forces acting on the infinitesimal element [36].

$$\left.\begin{aligned} \frac{\partial (\rho u)}{\partial t} + \frac{\partial (\rho u^2)}{\partial x} + \frac{\partial (\rho u v)}{\partial y} &= -\frac{\partial p}{\partial x} + \mu\left(\frac{\partial^2 u}{\partial x^2} + \frac{\partial^2 u}{\partial y^2}\right) + \rho f_x \\ \frac{\partial (\rho v)}{\partial t} + \frac{\partial (\rho u v)}{\partial x} + \frac{\partial (\rho v^2)}{\partial y} &= -\frac{\partial p}{\partial x} + \mu\left(\frac{\partial^2 v}{\partial x^2} + \frac{\partial^2 v}{\partial y^2}\right) + \rho f_y \end{aligned}\right\} \tag{3}$$

where, p [P$_a$] is the pressure on the infinitesimal body.

To better capture the dynamics of the process, this experiment utilizes the Realizable k-ε model for simulation, with the turbulence kinetic energy equation as follows [37]:

The transport equation for turbulence kinetic energy is:

$$\frac{\partial (\rho k)}{\partial t} + \frac{\partial (\rho k u_j)}{\partial x_i} = \frac{\partial}{\partial x_i}\left[(\mu + \frac{\mu_t}{\sigma_k})\frac{\partial k}{\partial x_j}\right] + G_k + G_b - \rho\varepsilon - Y_M + S_k \tag{4}$$

The transport equation for the turbulent dissipation rate is given by:

$$\frac{\partial (\rho \varepsilon)}{\partial t} + \frac{\partial (\rho \varepsilon u_j)}{\partial x_j} = \frac{\partial}{\partial x_j}\left[(\mu + \frac{\mu_t}{\sigma_\varepsilon})\frac{\partial \varepsilon}{\partial x_j}\right] + \rho C_1 S\varepsilon - \rho C_{2\varepsilon}\frac{\varepsilon^2}{k + \sqrt{\nu\varepsilon}} + C_{1\varepsilon}\frac{\varepsilon}{k}C_{3\varepsilon}G_b + S_\varepsilon \tag{5}$$

where, μ_t is the turbulent viscosity, σ_k and σ_ε are the turbulent Prandtl numbers corresponding to the turbulent kinetic energy k and the dissipation rate ε, with values of 1.0 and 1.3, respectively, G_k is the turbulent kinetic energy generated by the laminar velocity gradient, S_k and S_ε are user-defined turbulent kinetic energy and turbulence dissipation source terms, both set to 0, $C_{1\varepsilon}$, $C_{2\varepsilon}$ and $C_{3\varepsilon}$ are constants with values of 1.44, 1.9, and 1.92, respectively.

The establishment of the porous medium model satisfies the fluid flow equations with momentum sources, adhering to Darcy's law [38]. Once the fluid domain is defined as a porous medium, resistance coefficients can be artificially specified in each direction to account for the resistance of the solid phase to the fluid in the porous medium. The porous medium used in this experiment is assumed to be homogeneous, described by the following expression:

$$S_i = -(D\mu v_i + C_2\rho|v|v_i) \tag{6}$$

where, S_i is the source term in the momentum equation for the $i(x、y、z)$. D is the viscous resistance coefficient, defined as $\frac{1}{\alpha}$, α is the permeability; C_2 is the inertial resistance coefficient.

3.1.2 Fundamental Principles of Numerical Simulation

To simplify the calculations, a two-dimensional planar simulation model was established based on the cross-section of the measurement points, with relevant boundary conditions set as shown in Fig.4. The model dimensions were designed according to the experimental setup, measuring 400 mm in length and 600 mm in width. The filter thickness is 45 mm, and a porous medium model was utilized with an average density of 1.2 kg/m³ and a porosity of 0.27. An air inlet channel measuring 100 mm × 10 mm was created at the outlet position. To reduce the computational load while ensuring the accuracy of the simulation results, a steady-state solver was employed, with a maximum of 1000 iterations and a relative tolerance set to 0.1. Finally, the model's accuracy was verified by varying the length and angle of the guiding plates, followed by multiple numerical simulations.

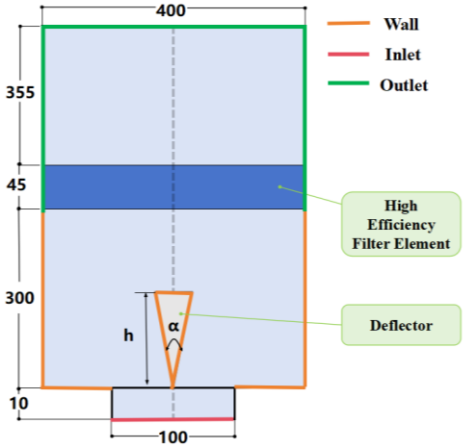

Fig.4 The schematic diagram of the two-dimensional simulation model.

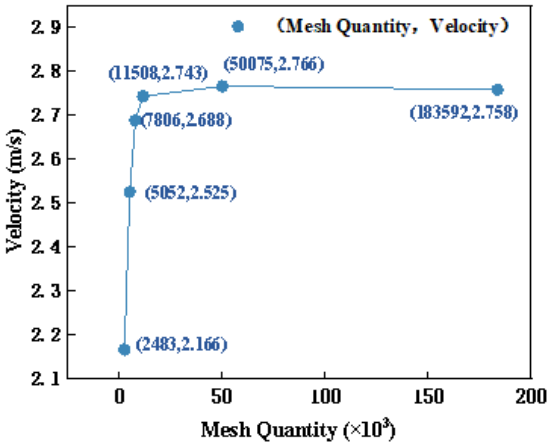

Fig.5 Grid independence analysis.

3.1.3 Grid Independence Analysis

Theoretically, an increased number of grid cells enhances grid quality. However, an excessive number of grid cells can consume computational resources and extend computation time. Conversely, having too few grid cells may adversely affect the accuracy of numerical results. To mitigate the larger errors that could arise from grid-related issues, this study selected six different numerical models with varying grid counts under the same operating conditions (with a deflector angle of 10° and a length of 10 mm) for numerical simulation. Based on the velocity calculations at a specific point, an appropriate grid count was determined. According to the results in Tab.3 and Fig.5, a model grid with 50,075 elements was chosen, balancing computational efficiency and result accuracy.

Tab.3 The velocity at a specific point under the same conditions with different grid resolutions.

Mesh Quantity	2483	5052	7806	11805	50075	183592
Velocity（m/s）	2.166	2.525	2.688	2.743	2.766	2.758

3.2. Machine Learning Methods

Previous studies have demonstrated that the gas flow within air purification models is complex, and its flow characteristics are influenced by the geometric structure of the guiding plates. However, existing research largely focuses on the effects of single variables under predefined conditions for

specific structures, revealing clear methodological limitations. Although some scholars have attempted to broaden their research scope through comprehensive numerical simulations or experimental analyses, these approaches are often time-consuming, labour-intensive, and costly. Furthermore, when faced with large parameter spaces, it becomes challenging to effectively explore global optimal solutions. Additionally, optimization design selections based on limited experimental or simulation results often struggle to accurately assess the potential performance improvements. To address these issues, this study proposes employing a machine learning approach that integrates genetic algorithms to optimize neural network parameters, facilitating collaborative optimization of the objective function within its continuous domain [39]. The optimized neural network will be able to learn the structural parameters of the guiding plates and subsequently analyze the impact of the guiding plate dimensions on the usage rate of air purifier filters.

3.2.1 Principles of Machine Learning

In recent years, machine learning methods have been widely utilized in various research areas for predictive purposes, achieving significant results [40]. Neurons are the basic units in neural networks, which receive multiple input signals, generate output signals through certain calculations and transmit the output signals to other neurons. The formula of neurons can be expressed as:

$$a = g\left(\sum_{i=1}^{n} w_i\, x_i + b\right) \tag{7}$$

$$g(z) = \max(0, z) \tag{8}$$

where, a is the output of the neuron, w_i is the weight of the $\mathrm{i}-\mathrm{th}$ input signal, x_i is the $\mathrm{i}-\mathrm{th}$ input signal, b is the bias, $g(z)$ is the ReLU activation function, which is used to map the input z of neurons to a specific output value for nonlinear transformations.

The core of this approach lies in employing multilayer neural networks for data modeling and feature extraction. Through its hierarchical structure, machine learning can automatically learn and extract multiple levels of abstract features from raw data, enabling efficient and accurate predictions and classifications in complex tasks [41]. This study aims to leverage this advanced technology to accurately predict the velocity non-uniformity coefficient and filter usage rate of a specific air purification model.

3.2.2 Selection of Machine Learning evaluation Indicators

Careful selection of the structural parameters of the guide vane can effectively alleviate the issues of uneven air supply and insufficient filter usage efficiency, thereby extending the filter's lifespan and maximizing its performance. In fluid dynamics, the distribution of flow field velocities can be assessed using uniformity indices based on area-weighted average velocity and mass-weighted average velocity [23, 42]. To further optimize the uniformity of air supply and the utilization efficiency of the purifier, this study employs the velocity non-uniformity coefficient K and filter usage rate as the primary evaluation metrics, reflecting the fluid velocity distribution characteristics across the entire flow cross-section and analyzing the impact of guide vane dimensions on the air purifier's filter usage rate. The calculation method for the velocity non-uniformity coefficient is as follows [6]:

$$K = \frac{\xi}{\zeta} \tag{9}$$

$$\xi = \sqrt{\frac{1}{n}\sum_{i=1}^{n}(f_i - \zeta)^2} \tag{10}$$

$$\zeta = \frac{1}{n}\sum_{i=1}^{n} f_i \tag{11}$$

where, K the velocity non-uniformity coefficient, ξ the root means square deviation of the velocity at the windward surface measurement points of the filter element, ζ is the weighted average velocity at the same measurement points. A smaller K value indicates better airflow distribution uniformity.

The calculation method for the filter element utilization rate δ is as follows [43]. It characterizes the degree of deviation between the observed values at the windward surface measurement points and the maximum value. A larger δ indicates better filter utilization and a longer lifespan.

$$\delta = 1 - \frac{\sum_{i=1}^{n}\left(\frac{Q_{max} - Q_i}{Q_{max}}\right)}{n} \tag{12}$$

where, Q_i [m^3h^{-1}]is the airflow through each filter section, Q_{max} [m^3h^{-1}] is the maximum airflow through the filter section.

When both the velocity non-uniformity coefficient is minimized and the filter utilization rate is maximized, it signifies that the structural parameters of the guide vanes have the most significant impact on promoting airflow uniformity in the purifier and extending the filter's lifespan. Therefore, a comprehensive evaluation index β is introduced to further refine the optimal selection of guide vane structural parameters.

$$\beta = \frac{\delta}{K} \tag{13}$$

4. Results and discussion

4.1. Experimental Results on the Impact of Baffle Structural Parameters on Air Purifier Performance

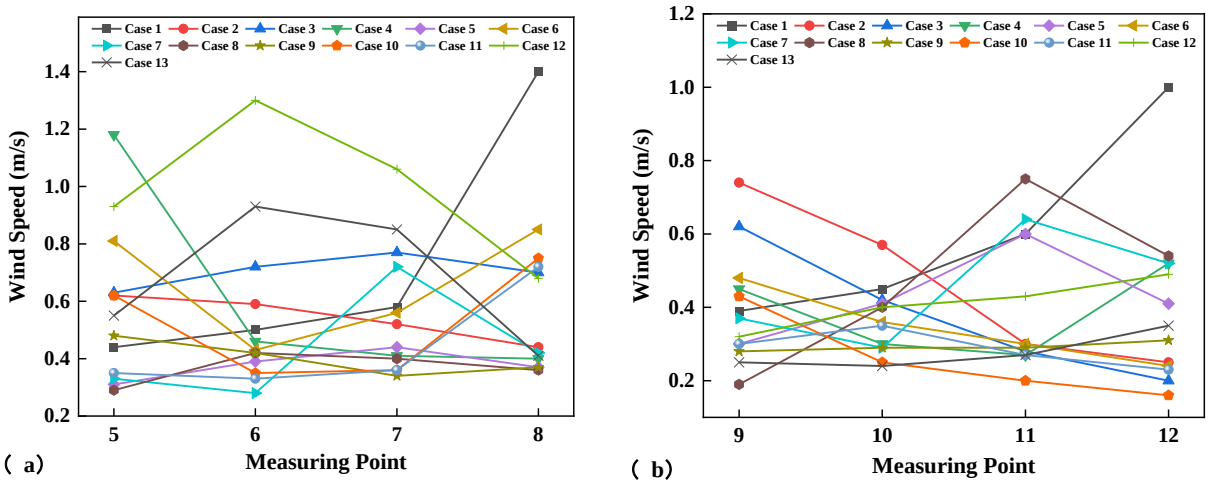

Fig.6 The wind speed measurement data for flow cross-sections 2 and 3. (a) Flow cross-sections 2 (b) Flow cross-sections (Windward face)

The influence of various baffle structural parameters on air purifier performance is primarily assessed through the analysis of data from the areas in front of the windward surface, specifically the test results from measurement points 1 to 12. However, under certain conditions with longer baffle lengths or larger angles (conditions 8 to 13), the physical constraints limit the ability of the hot-wire anemometer to penetrate the baffle structure, preventing effective data collection from measurement points 1 to 4 (flow cross-section 1). In light of this limitation, this experiment organizes the data from measurement points 5 to 12 (flow cross-sections 2 and 3) for each condition, as illustrated in Fig.6.

Based on Fig.6 (a) and (b), it can be observed that the air velocity decreases as the distance from the wind opening increases, and the overall trend of the two cross-sections is relatively consistent across most cases. Specifically, cases 9 to 11 exhibit relatively low average wind speeds; at cross-section 2, case 12 has the highest average wind speed, followed by cases 1 and 3. On the windward side, case 1 has the highest average wind speed, followed by cases 2 and 8. Fig.7 provides a detailed illustration of the wind speed variance for each condition at cross-sections 2 and 3. The data presented in the Fig.7 indicate that case 5 has the smallest wind speed variance at cross-section 2, at 0.0029, while case 9 shows the lowest variance on the windward side, approximately 0.0002.

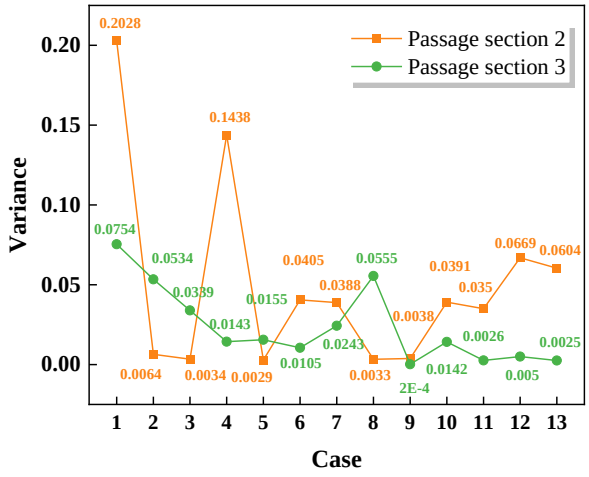

Fig.7 The variance of wind speed in the wind speed sampling plane.

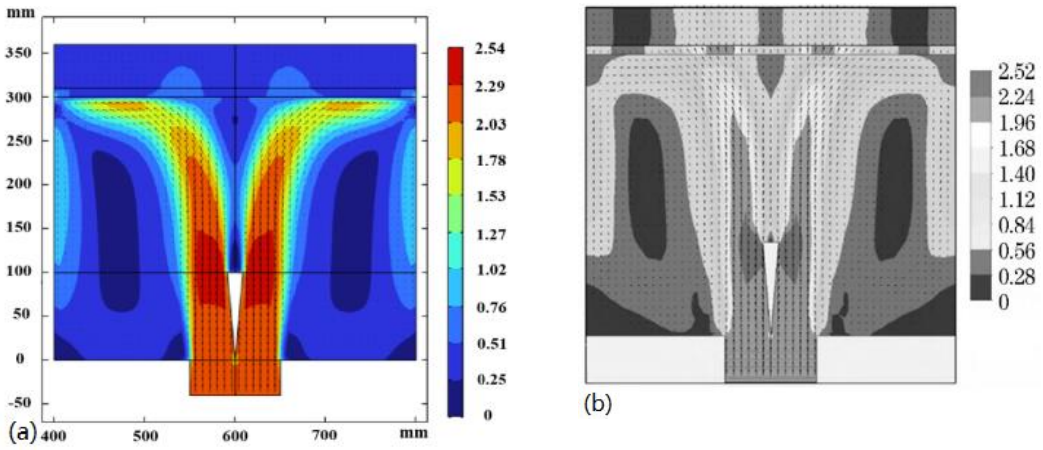

Fig.8 Comparison of velocity vector diagrams under case 6. (a) For the current case 6 (b) For other scholars' case 6 [44]

4.2. Numerical Model Validation

This study conducts simulation experiments using COMSOL Multiphysics software, focusing on Condition 6 with the corresponding parameter settings. The velocity vector diagram is shown in Figure 8 (a). To validate the model's effectiveness, the results obtained are compared with the simulated velocity vector diagram from other researchers under the same conditions, as illustrated in Figure 8 (b) [44]. Analysis reveals that the error between the two sets of results remains within a reasonable range, strongly supporting the accuracy and validity of the simulation model developed in this study.

By varying the length and angle of the deflector plates, this study conducted a total of 200 simulation experiments, resulting in a comprehensive dataset that encompasses multiple deflector plate configuration scenarios. The non-uniformity of velocity and filter utilization rates are as follows:

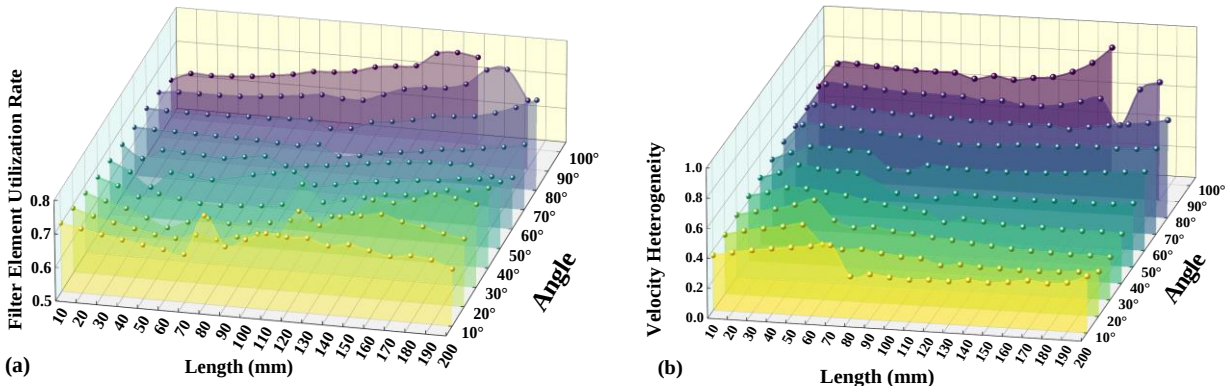

Fig.9 Filter element utilization and velocity uniformity under various operating conditions. (a) Filter element utilization (b) Velocity uniformity

Fig.9 (a) shows that when the length of the deflector plates is between 10 and 110 mm, an increase in the angle of the deflector plates generally leads to a gradual decrease in filter utilization rates, although a significant spike occurs at angles of 40° or 50°. In contrast, when the length of the deflector plates is between 120 and 200 mm, the filter utilization rate exhibits a trend of initially increasing, then decreasing, and subsequently increasing again as the angle increases. These results indicate that deflector plates with smaller angles facilitate fluid diversion, while longer deflector plates tend to direct the fluid closer to the windward side. Therefore, a deflector plate angle of 10° with a length between 150 and 200 mm results in higher filter utilization rates.

According to Fig.9 (b), when the length of the guide plate remains constant, an increase in the angle of the guide plate generally leads to a rising trend in velocity uniformity. In this case, the optimal angle is found to be evenly distributed around 10° or 20°. Conversely, when the angle of the guide plate is fixed, increasing the length of the guide plate results in a complex variation of velocity uniformity, initially increasing, then decreasing, and finally increasing again. This phenomenon indicates that the length of the guide plate must be appropriately moderate; when the guide plate is too short, its guiding capability is limited, rendering it ineffective in directing the fluid toward the windward side. Conversely, if the guide plate is too long, although its guiding capability improves, it also increases the resistance to fluid flow, leading to a decrease in overall efficiency. An optimal performance is observed when the guide plate length is between 80 and 120 mm.

In scenarios with high filter utilization and low-velocity non-uniformity, the design of the guide plate structure significantly enhances airflow uniformity and prolongs filter life. Fig.10 illustrates the scatter distribution of the two evaluation metrics along the central axis. By focusing on data-dense regions, the central axis is set with a horizontal coordinate of 0.5 and a vertical coordinate of 0.7; data points closer to the upper left corner indicate superior performance. The first quadrant contains 30 data points, with the optimal configurations marked by the red dashed line representing five conditions. Based on Eq.(13), a comprehensive evaluation metric for different conditions is presented in Fig.11. The region with favorable metrics is defined within the range of $10° \leq \alpha \leq 40°$, $80mm \leq h \leq 200mm$, resulting in a comprehensive evaluation metric range of $2.0 \leq \beta \leq 2.8$.

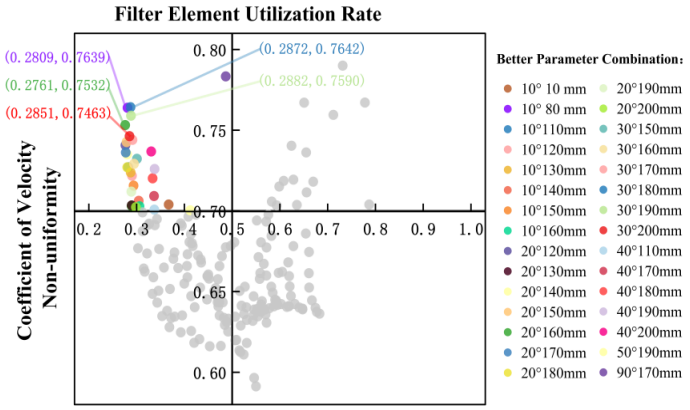

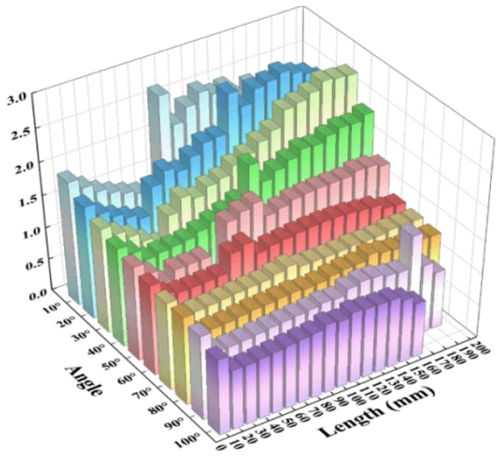

Fig.10 Evaluation metric axial scatter distribution. **Fig.11 Comprehensive evaluation metric.**

Figure 12 presents a comparison of experimental and simulation values for all detectable measurement points under 13 different operating conditions, totaling 132 valid data points. Among these, 70.45% of the simulation values closely match the experimental values, with 10% of the data having an error within 1%. Additionally, 28% of the data maintains an error within 5%, while 37% of the data shows an error of no more than 10%.

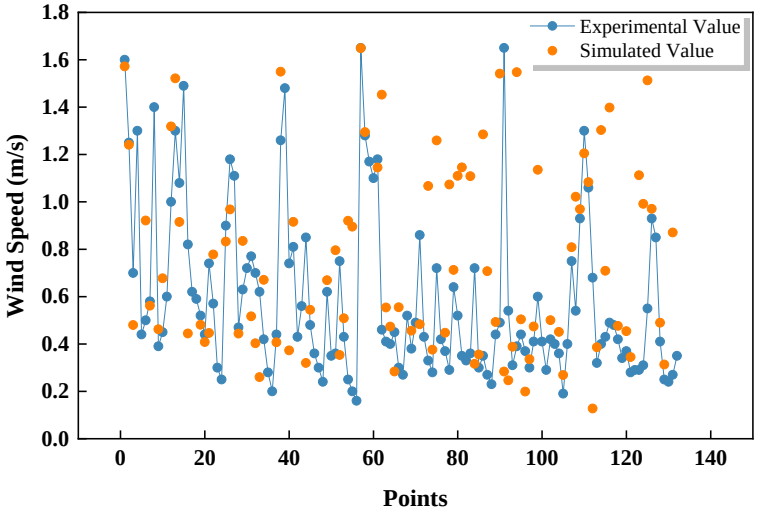

Fig.12 Experimental and simulation values at all measurement points under all operating conditions.

4.3. Machine Learning Predictions

In this study, a five-layer neural network structure (2-100-20-5-1) is constructed using PyTorch. The length and angle of the glass fiber filter's baffle plate serve as input features for the two neurons in the input layer. Additionally, this network structure includes three hidden layers with 100,

20 and 5 neurons respectively, which are responsible for extracting abstract features from the input data and learning complex nonlinear mappings. Ultimately, the output layer contains one neuron used to predict the velocity uniformity coefficient and filter element utilization rate of the glass fiber filter. The network adopts a fully connected architecture, allowing the model to capture complex nonlinear relationships between input features and output targets for optimal performance [45].

The ReLU activation function is employed to generate sparse activation patterns, enhancing the neural network's nonlinear fitting capability [46]. Subsequently, the data is split into a training set and a test set in a ratio of 0.8 : 0.2. The Adam optimizer is employed with a total of 1000 iterations, and the data splitting method follows the same approach as the width learning dataset, allocating 80% to the training set and 20% to the testing set. After training the model on the training set, the predictions for the coefficient of velocity uniformity and filter element utilization on the testing set are illustrated in Fig.13. The results indicate that the predicted values closely align with the actual values, suggesting that the proposed predictive model demonstrates a high level of accuracy.

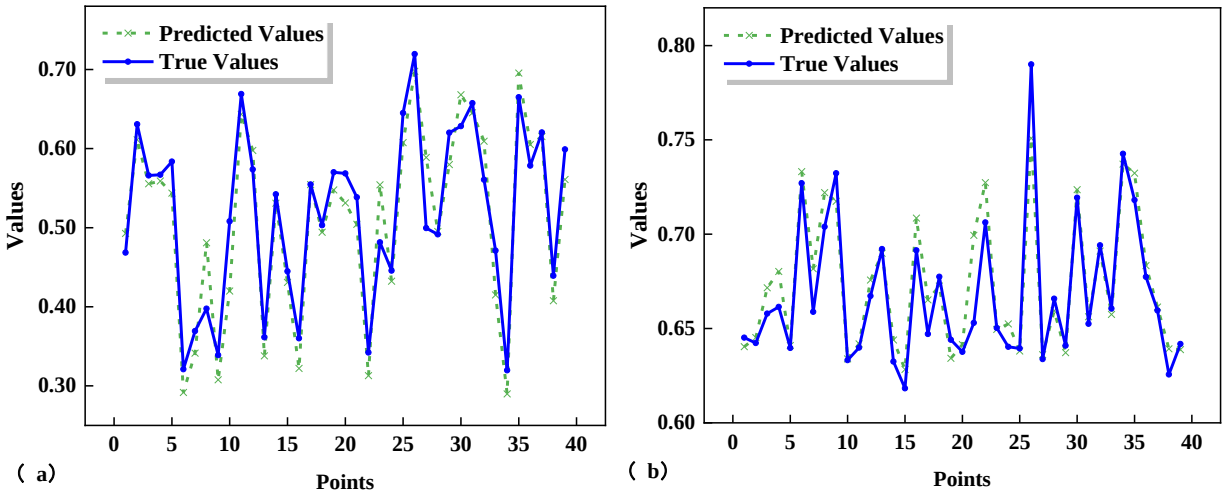

Fig.13 The predictive performance of the neural network model for the coefficient of velocity non-uniformity and the filter element utilization rate. (a) Coefficient of Velocity Non-uniformity (b) Filter Element Utilization Rate

The advantage of Bayesian optimization lies in its ability to reduce the number of evaluations required to find the optimal solution by intelligently selecting evaluation points, particularly in scenarios where the evaluation cost is high [47]. This approach applies to various machine learning algorithms and models, enhancing model performance and improving generalization capabilities on validation data. Furthermore, it significantly simplifies the complexity of the parameter-tuning process, demonstrating broad applicability [48]. In this study, a surrogate model was constructed using the Bayesian optimization method, which effectively identifies the global optimum by iteratively selecting the best parameters. This method automatically generates expected optimal parameters and iteratively adjusts them within the neural network model until a superior combination is found, thereby achieving the dual objectives of minimizing the coefficient of velocity non-uniformity and maximizing the filter element utilization rate.

The predictive results indicate that when the velocity non-uniformity is minimized (0.3), the corresponding length and angle are 163.2 mm and 38.5°, respectively. Conversely, when the filter element utilization rate is maximized (0.77), the length and angle are 123.4 mm and 39.8°.

Additionally, when the angle of the guide plate is 61° and the length is 105.25 mm, the overall performance of the air purification model is optimal. Based on the numerical set of comprehensive evaluation indicators, the predictive results from the Bayesian optimization method show that the air purification model performs best when the guide plate angle is 11° and the length is 81 mm. In total, four sets of predictive results are presented, as shown in Tab.4.

Tab.4 The prediction results of machine learning.

	Result 1	Result 2	Result 3	Result 4
Length（mm）	163.2	123.4	105.25	81
Angle（° ）	38.5	39.8	61	11
Velocity heterogeneity	0.277586638	0.335766851	0.422923889	0.352624431
Filter element utilization rate	0.768055395	0.655666185	0.637977379	0.658176039

After comparative analysis, the structural parameters of the four groups of baffles are closely aligned with the five optimal operating conditions described in Section 4.2. Reintroducing these parameters into the simulation yields specific values for the velocity uniformity coefficient and filter usage rate, as shown in the table. Notably, result 1 indicates the minimum velocity non-uniformity and the maximum filter usage rate. Therefore, the optimal baffle structural parameters can be selected as a length h of 163.2 mm and an angle α of 38.5°, yielding a comprehensive evaluation index of approximately 2.767, the highest value across all simulated conditions.

5. Conclusions

This study provides a comprehensive analysis of how diffuser structure parameters impact the performance of air filtration systems, thereby enriching the theoretical framework of airflow control and filtration efficiency optimization. Through a combination of experimental measurements and numerical simulations, we have systematically examined the mechanisms through which diffuser structural parameters influence the air delivery system's uniformity and lifespan. Furthermore, we have developed a machine learning-based predictive model for diffuser performance, which accurately delineates the interplay between structural parameters, airflow uniformity, and filter lifespan, yielding optimal parameters that offer substantial theoretical and technical insights for related industries. The main conclusions are as follows:

(1) A strong correlation between experimental and simulation results, with 10% of the data exhibiting a 1% error, 28% within a 5% error margin, and 37% with errors not exceeding 10%.

(2) The determination of an optimal range for diffuser structures based on simulation outcomes, establishing a comprehensive evaluation index range.

(3) The application of Bayesian optimization has significantly improved the neural network model's performance, enabling more precise predictions of diffuser structural parameters. The optimal parameters identified were a diffuser length of 163.2 mm and an angle of 38.5°, corresponding to a comprehensive evaluation index of approximately 2.767.

Acknowledgement

This research work is supported by the Funding project of Jimei University Scientific Research Startup Fund (ZQ2023023) and the Natural Science Foundation of Fujian Province (2021J10854).

References

[1] Rana, A.K., *et al.*, Cellulose-based materials for air purification: A review, *Industrial Crops and Products, 194*. (2023),

[2] Liu, G., *et al.*, A review of air filtration technologies for sustainable and healthy building ventilation, *Sustainable Cities and Society*, *32*. (2017), pp. 375-396.
[3] González-Martín, J., *et al.*, A state–of–the-art review on indoor air pollution and strategies for indoor air pollution control, *Chemosphere*, *262*. (2021), p. 128376.
[4] Le, T.S., *et al.*, Air purification equipment combining a filter coated by silver nanoparticles with a nano-TiO2 photocatalyst for use in hospitals, *Advances in Natural Sciences: Nanoscience and Nanotechnology*, *6*. (2015), 1
[5] Hyun Min Kim, Evaluation for Infection Control and Indoor Environmental Impact for Temporary Negative Pressure Isolation (TNPI) Chamber in Emergency Wards, Graduate School of Seoul National University,2024.
[6] Lian, Z., *et al.*, Presentation and evaluation of a new type of air supply system in a passenger carriage in China, *Applied Thermal Engineering*, *24*. (2004), 5-6, pp. 703-715.
[7] Knibbs, L.D., *et al. AUTOMOBILE HVAC SYSTEMS : AIR FLOW , LEAKAGE AND THEIR EFFECTS ON IN-VEHICLE AIR QUALITY*,2008,
[8] Vijayan, V.K., *et al.*, Enhancing indoor air quality –The air filter advantage, *32*. (2015), pp. 473 - 479.
[9] Zhang, M., *et al.*, Evaluation and prediction of fibrous filters' operating performance in residential fresh air system, *Building and Environment*, *255*. (2024), p. 111441.
[10] Yit, J.E., *et al.*, Empirical modelling of filtration performance for the fibrous air filters with final resistance recommendation, *Results in Engineering*, *16*. (2022),
[11] Afifa, *et al.*, Air pollution and climate change as grand challenges to sustainability, *Science of The Total Environment*, *928*. (2024), p. 172370.
[12] Li, S., *et al.*, Application and research of dry-type filtration dust collection technology in large tunnel construction, *Advanced Powder Technology*, *28*. (2017), 12, pp. 3213-3221.
[13] Cutler, T.D.,J.J. Zimmerman, Ultraviolet irradiation and the mechanisms underlying its inactivation of infectious agents, *Animal Health Research Reviews*, *12*. (2011), 1, pp. 15-23.
[14] Sharma, S., *et al.*, An overview on recent progress in photocatalytic air purification: Metal-based and metal-free photocatalysis, *Environmental Research*, *214*. (2022), p. 113995.
[15] Wang, Z.,J.S. Zhang, Characterization and performance evaluation of a full-scale activated carbon-based dynamic botanical air filtration system for improving indoor air quality, *Building and Environment*, *46*. (2011), 3, pp. 758-768.
[16] Ghosh, N.K., *et al.*, Particle Pollution with PM 2.5, Reduction of Indoor Aeroallergen and Overall Particle Count Using AHPCO and Plasma Hybrid Technology for Air Purification, *Journal of Allergy and Clinical Immunology*, *143*. (2019), 2, p. AB74.
[17] Zhang, X., *et al.*, Establishment of air fiber filtration model based on fractal theory and analysis of filtration performances, *Materials Today Communications*, *34*. (2023), p. 105301.
[18] Bardin‐Monnier, N.,D. Thomas. *Initial Pressure Drop for Fibrous Media*,2017,
[19] Wang, A., *et al.*, High efficiency, low resistance and high temperature resistance PTFE porous fibrous membrane for air filtration, *Materials Letters*, *295*. (2021) 129831,
[20] Li, S., *et al.*, Influence of pleat geometry on the filtration and cleaning characteristics of filter media, *Separation and Purification Technology*, *210*. (2019), pp. 38-47.
[21] Alilou, Y., *et al.*, Airflow characterization within the pleat channel of HEPA filters with mini pleats, *The Canadian Journal of Chemical Engineering*, *99*. (2021), S1, pp. S693-S702.
[22] Teng, G., *et al.*, Influence of pleated geometry on the pressure drop of filters during dust loading process: experimental and modelling study, *Scientific Reports*, *12*. (2022), 20331
Zhang , Y.Y., RAN Jingyu, XIU Hengxu, Numerical simulation of flow distribution uniformity in TWC and optimal design of catalyst in CNG vehicle, *56*. (2005), 9, pp. 1679-1684.
[24] Zhuang, C., *et al.*, Optimization of the Structure of a Solar Air Heater Fitted with V-Shaped Perforated Baffles, *International Journal of Heat and Technology*, *34*. (2016), 4, pp. 604-610.
[25] Menni, Y.,A. Azzi, DESIGN AND PERFORMANCE EVALUATION OF AIR SOLAR CHANNELS WITH DIVERSE BAFFLE STRUCTURES,*Computationl Thermal Science*, *10*. (2018), 3, pp. 225-249.
[26] Shuqi, Z., *et al.*, Artificial neural network-based optimization of baffle geometries for maximized heat transfer efficiency in microchannel heat sinks, *Case Studies in Thermal Engineering*, *49*. (2023), p. 103331.

[27] Li, J.-L., *et al.*, Numerical simulation and thermal performance optimization of turbulent flow in a channel with multi V-shaped baffles, *International Communications in Heat and Mass Transfer*, *92*. (2018), pp. 39-50.
[28] Luo, Z.T.-F., Zhang Y-F,Bao M,Yu G-C, *Optimal design of air purifier filter element based on CFD*, *Proceedings of China Household Appliance Technology Conference 2020*. 2020: Linbo, China. p. 1521-1524.
[29] Cheng, K., *et al.*, CFD–DEM simulation of particle deposition characteristics of pleated air filter media based on porous media model, *Particuology*, *72*. (2023), pp. 37-48.
[30] Xu, L.J.-C., Su F,Dong Y-D, Structure improvement and flow performance analysis of air purifier, *Journal of Xi'an Polytechnic University*, *32*. (2018), 2, pp. 216-221,236.
[31] Shi, T., *et al.*, Novel process optimization based on machine learning: A study on biohydrogen production from waste resources, *Biomass and Bioenergy*, *185*. (2024), p. 107222.
[32] Alli, Y.A., *et al.*, Optimization of 4D/3D printing via machine learning: A systematic review, *Hybrid Advances*, *6*. (2024), p. 100242.
[33] Santagata, T., *et al.*, Modelling and experimental characterization of unsaturated flow in absorbent and swelling porous media, *Chemical Engineering Science*, *224*. (2020), p. 115765.
[34] Jafari, A., *et al.*, An eXtended finite element method implementation in COMSOL multiphysics: Thermo-hydro-mechanical modeling of fluid flow in discontinuous porous media, *Computers and Geotechnics*, *159*. (2023), p. 105458.
[35] Santamaría Bertolín, L., *et al.*, Optimal position of air purifiers in elevator cabins for the improvement of their ventilation effectiveness, *Journal of Building Engineering*, *63*. (2023), p. 105466.
[36] Tryggvason, G., *Chapter 6 - Computational Fluid Dynamics*, in: *Fluid Mechanics (Sixth Edition)*, (Ed., Editor^Editors), Academic Press: Boston. 2016, pp. 227-291.
[37] Wang, F., *et al.*, The Turbulent Schmidt Number for Transient Contaminant Dispersion in a Large Ventilated Room Using a Realizable k-ε Model, *Fluid Dynamics and Materials Processing*, *20*. (2024), 4, pp. 829-846.
[38] Hernandez-Rodriguez, R., *et al.*, Momentum transport in the free fluid-porous medium transition layer: one-domain approach, *Chemical Engineering Science*, *248*. (2022), p. 117111.
[39] Fang, J., *et al.*, Machine learning accelerates the materials discovery, *Materials Today Communications*, *33*. (2022), p. 104900.
[40] Hu, Y., *et al.*, Fusion dynamical systems with machine learning in imitation learning: A comprehensive overview, *Information Fusion*, *108*. (2024), p. 102379.
[41] Jiang, Q., *et al.*, Hybrid multilayer perceptron and convolutional neural network model to predict extreme regional precipitation dominated by the large-scale atmospheric circulation, *Atmospheric Research*, *304*. (2024), p. 107362.
[42] Tao, H.-G., *et al.*, An alternative approach to quantifying fluid flow uniformity based on area-weighted average velocity and mass-weighted average velocity, *Energy and Buildings*, *45*. (2012), pp. 116-123.
[43] Zhong, X.Z.L.W.U.C.-b., Experiments and Numerical Simulation of Flow Distribution with Larger Flux in Multi-branch Pipe, *JOURNAL OF CHONGQING UNIVERSITY*, *29*. (2006), 1, p. 41.
[44] L-Y, S., *et al.*, Optimization of the baffle structure of plasma generator %J Journal of Harbin University of Commerce(Natural Sciences Edition), *40*. (2024), 1, pp. 57-63.
[45] Zhang, R., *et al.*, Review of Deep Learning, *abs/1804.01653*. (2018),
[46] Sudjianto, A., *et al.*, Unwrapping The Black Box of Deep ReLU Networks: Interpretability, Diagnostics, and Simplification, *abs/2011.04041*. (2020),
[47] Yang, L., *et al.*, A local space transfer learning-based parallel Bayesian optimization with its application, *Chinese Journal of Chemical Engineering*, *74*. (2024), pp. 227-237.
[48] Scyphers, M.E., *et al.*, Bayesian Optimization for Anything (BOA): An open-source framework for accessible, user-friendly Bayesian optimization, *Environmental Modelling & Software*, *182*. (2024), p. 106191.

Submitted: 18.11.2024.
Revised: 18.01.2025.
Accepted: 19.01.2025.